Fully Automatic Luminal Contour Segmentation in Intracoronary Ultrasound Imaging—A Statistical Approach

Elisabeth Brusseau*, Chris L. de Korte, Frits Mastik, Johannes Schaar, and Anton F. W. van der Steen

***Abstract*—In this paper, a fully automatic method for luminal contour segmentation in intracoronary ultrasound imaging is introduced. Its principle is based on a contour with *a priori* properties that evolves according to the statistics of the ultrasound texture brightness, which is generally Rayleigh distributed. The main interest of the technique is its fully automatic character. This is insured by an initial contour that is not set by the user, like in classical snake-based algorithms, but estimated and, thus, adapted to each image. Its estimation combines two pieces of information extracted from the *a posteriori* probability function of the contour position: the function maximum location (or maximum *a posteriori* estimator) and the first zero-crossing of its derivative. Then, starting from the initial contour, a region of interest is automatically selected and the process iterated until the contour evolution can be ignored.**

***In vivo* coronary images from 15 patients, acquired with the 20-MHz central frequency Jomed Invision ultrasound scanner, were segmented with the developed method. Automatic contours were compared to those manually drawn by two physicians in terms of mean absolute difference. The results demonstrate that the error between automatic contours and the average of manual ones is of small amplitude, and only very slightly higher (0.099 ± 0.032 mm) than the interexpert error (0.097 ± 0.027 mm).**

***Index Terms*—Active contour, coronary artery, echo envelope statistics, intravascular ultrasound, Rayleigh distribution, segmentation, snakes.**

I. Introduction

SEGMENTATION of deformable structures is a common processing problem in medical imaging. For example, coronary atherosclerosis severity is mainly deduced from the degree of vessel stenosis, induced by the atherosclerotic plaque formation [1]–[3]. It is generally estimated, from intravascular ultrasound (IVUS) images, by segmenting and measuring the lumen area, and by referencing it to the total cross-sectional area of the vessel. With the majority of IVUS systems, this work is generally manually performed. However, due to the tedious nature of manual tracing, many research groups have worked on developing semi-automatic and automatic segmentation methods.

In this paper, we present a new fully automatic segmentation method for endoluminal contour detection in intracoronary ultrasound images. This method has been developed in the framework of preprocessing for intravascular elastography. However, the method can be directly used for measuring the lumen area. Intravascular elastography is an emerging technique whose aim is to provide clinicians with a map of the arterial wall deformation during the cardiac cycle [4]–[6]. Arterial wall strain distribution is estimated by tracking changes in the received signals, induced by the blood pressure variation. Because the transducer is positioned within the lumen and not in direct contact with the vessel wall, the first part of the acquired RF signals corresponds to echoes from blood, and the second part to echoes from tissue. In order to assess arterial wall strain, the blood-wall interface must first be delineated. IVUS elastography might provide useful information on mechanical characteristics of plaques and, thus, might be helpful to select the most appropriate treatment course and to predict the disease evolution. It has also potential interest for the investigation of plaque vulnerability, since the rupture process is correlated with plaque composition, morphology, and mechanical properties [7]–[12]. With the development of real-time three-dimensional (3-D) elastography, a robust and fully automatic endoluminal contour segmentation is prerequisite.

Many research groups have investigated contour detection applied to medical images and in particular, to IVUS images. The first reported works dealt with techniques that exploited only the image characteristics to segment structures. For instance, gradient-based algorithms identify, at each angular position, the contour as the location of the maximum pixel intensity variation. These techniques have been successfully implemented in many fields of image processing [13]. However, when applied to ultrasound images, their performance are degraded by a potentially low contrast between blood and tissue and by low signal-to-noise ratios (SNRs). Indeed ultrasound images are characterized by a speckle noise, that is responsible for many comparatively strong gradients throughout the whole image. The gradient is a too local feature to discriminate between noise and diffuse actual boundaries. Consequently, the endoluminal contour is successfully detected only in regions where the blood-wall interface corresponds to a significant pixel intensity variation. For low contrast interface regions, the contour detection fails rapidly.

Manuscript received July 25, 2003; revised January 12, 2004. The work of F. Mastik was supported by the Dutch Technology Foundation STW. The work of J. Schaar was supported by the Deutsch Hertzstiftung and the Dutch Heart Foundation. The Associate Editor responsible for coordinating the review of this paper and recommending its publication was M. Insana. *Asterisk indicates corresponding author.*

*E. Brusseau is with the CREATIS UMR CNRS 5515, INSERM U630, Lyon, France.

C. L. de Korte, J. Schaar and A. F. W. van der Steen are with the Biomedical Engineering, Thorax Center, Erasmus Medical Center, 3015 GD Rotterdam, The Netherlands and also with the Interuniversity Cardiology Institute of The Netherlands (ICIN), 3501 DG Utrecht, The Netherlands.

F. Mastik is with the Biomedical Engineering, Thorax Center, Erasmus Medical Center, 3015 GD Rotterdam, The Netherlands.

Digital Object Identifier 10.1109/TMI.2004.825602

Another approach developed by Li *et al.* [14] exploited spatiotemporal properties of RF ultrasound signals to detect the endoluminal contour. The authors demonstrated that these properties permit an efficient separation between the echoes from the blood and those from the arterial wall. A temporal correlation method was used to evaluate the changes in RF signals, which were acquired from the same angle at a time interval of 200 μs. With such a temporal resolution, this method is easily able to discriminate between blood and vessel wall, since successive wall echoes remain highly correlated, while those from the blood show poor similarities. But with conventional ultrasound examinations, for which data are acquired at a time interval of 30 ms, the processing fails rapidly. This is simply due to the fact that, during this time interval, the vessel wall suffers from too much motion and it, thus, decorrelates as much as the blood.

Semi-automatic border detection techniques [15]–[22] have also been investigated. These are computer assisted tracing procedures that require input from experienced observers. Several strategies have been developed to integrate the expertise of humans into segmentation algorithms [19]. The differences in these strategies are the amount of time and effort required by an operator. Some procedures consist simply in manually placing markers along the searched contour, that serve as a guide to the segmentation algorithm [21]. Such techniques perform well but they are generally not suited for large population studies. Thus most programs first start with an automatically detected contour. Then, over regions where the segmentation has not led to the expected result, points are manually added or modified to force the contour passing through the desired location. Such techniques have notably been developed and validated for 3-D intracoronary ultrasound [17], [22]. These methods are less tedious than manual tracing, but in many cases require expert interaction.

For clinical practice, the most attractive approaches remain those based on a fully automatic processing. A method proposed by Sonka *et al.* [23]–[25], dedicated to the automatic segmentation of IVUS images, uses global image information and heuristic graph searching to identify wall and plaque borders. The authors have incorporated *a priori* knowledge on coronary artery anatomy and ultrasound image characteristics into the method. This technique is particularly advantageous for images in which local edge gradients are insufficient to reliably identify border positions. However, the authors underlined two limitations: the need to select a region of interest (ROI) prior to the automatic border detection, and the injected *a priori* knowledge that might be not applicable in all cases.

Most promising techniques appear to be those based on active contours or *snakes* [26]–[29]. The principle of active contours consists of defining an initial contour with *a priori* properties, in terms of shape, continuity, smoothness and then deforming it according to the image characteristics, until a cost function is minimized. In practical terms an initial contour, generally a circle, is set which then evolves according to its intrinsic properties and image features (image intensity, image gradient, …). A balloon force [30], [31] can also be added to force the contour to inflate or deflate, and prevent the contour from shrinking to a point. A related approach exploits textural or statistical differences between regions as the basis for active contour deformation [32], [33]. This leads to techniques that are very well suited to process noisy images like ultrasound images [34], [41]. They mainly model the envelope statistics in IVUS images by Rayleigh distributions [35]–[37], different regions being identified by different Rayleigh parameters. The searched contour is then the one that maximizes an *a posteriori* probability. This estimator was initially introduced by Dias and Leitao [38] for semi-automated contour detection of two heart boundaries.

Algorithm performance also depends on the selected *a priori* contour characteristics, for which several models have been proposed. The use of B-splines [39] permits the direct calculation of smooth contours. Using polygons leads to simple and fast algorithms, but requires the introduction of smoothness constraints [40]. The use of parametric equations makes the algorithm rapidly converge to a solution, but the set of allowed shapes of the searched contour must be specified [41].

These different algorithms lead to smooth final contours, which ignore isolated edges and overcome the problem of low contrast or noisy regions. However, there are a number of problems associated with these approaches such as the initialization of the contour, the selection of the ROI, the possible existence of multiple minima and the selection of the snake parameter values. It is well known that the parameters of such techniques are difficult to tune.

The aim of this paper is to present a fully automatic endoluminal contour segmentation algorithm we developed, that overcomes the previously stated limitations. Like the methods presented by Haas *et al.* and Guerault *et al.* [32], [33], our technique is based on an active contour that evolves until it optimally separates regions with different statistical properties. However, unlike these methods, our technique requires neither the preselection of an ROI tight around the search contour, nor the initialization of the contour close to its final position. This has been overcome by the integration of a process dedicated to the computation of the initial contour.

This paper is organized as follows: the theoretical framework of echo envelope statistics and bayesian estimation of the contour position is described in Section II, followed by the description of the method implementation in Section III. Results using images from 15 different patients are presented in Section IV. Section V provides a discussion of the results along with concluding remarks.

II. Theoretical Framework

The approach adopted in this study is mainly a statistical one. It exploits statistical differences in blood and tissue scattering to deform the contour. Consequently, it is of fundamental importance to first investigate the specific echo envelope statistics of the images.

A. Statistics of Ultrasound Echo Envelope

An inherent characteristic of ultrasound B-scans is the presence of speckle noise. Speckle is an interference pattern, resulting from the interaction between the ultrasound waves and the scatterers within the tissue. It has a stochastic nature since it is formed by the summation of echo signals from randomly

located scattering centers, each of which backscatters a random amount of energy. Statistics of ultrasound echo envelope have been a major subject of investigation [35], [36], [50]. It has been demonstrated that the statistics of the B-scan brightness depends mainly on the number of scatterers per resolution cell, and on the distribution law of the scatterers locations [41], [42], [43]. Three main models have been identified. The first is for fully developed speckle induced by a large number (> 10 per resolution cell) of randomly located scatterers, which is well modeled by a *Rayleigh probability density function* [32], [33], [41], [44], [45]. With this model, the probability that a pixel i has an amplitude A_i is given by

$$\mathrm{P(A_i)} = \frac{\mathrm{A_i}}{\alpha^2} \exp\left(-\frac{\mathrm{A_i^2}}{2\alpha^2}\right) \tag{1}$$

where α is the distribution parameter that needs to be estimated.

When a coherent component is introduced, for example by the presence of a regular structure of scatterers within the tissue, the B-scan brightness statistics can be approximated by a *Rician distribution* [42]

$$\mathrm{P(A_i)} = \frac{\mathrm{A_i}}{\alpha^2} \exp\left(-\frac{\mathrm{A_i^2 + s^2}}{2\alpha^2}\right) \mathrm{I_0}\left(\frac{\mathrm{sA_i}}{\alpha^2}\right) \tag{2}$$

where I_0 is the zeroth-order modified Bessel function of the first kind, and α and s are parameters to be estimated. The parameter s is relative to the coherent component. The group of Rician probability density functions is composed of distributions that evolve from the Rayleigh distribution when the coherent component is equal to zero, to the Gaussian distribution when the coherent component tends toward infinity.

Finally, partially developed speckles induced by a low effective number of scatterers can be modeled by a *K-distribution* (3) [41], [45]–[49]. The K-distribution family is composed of distributions that evolve from the exponential probability density function, when the scatterer density within the tissue tends to zero, to the Rayleigh distribution when the scatterer density becomes large. The K-distribution is, thus, a generalization of the Rayleigh distribution for small effective number of scatterers

$$\mathrm{P(A_i)} = \frac{2\mathrm{b}}{\Gamma(\alpha)} \left(\frac{\mathrm{bA_i}}{2}\right)^{\alpha} \mathrm{K_{\alpha-1}(bA_i)} \quad \mathrm{b} = 2\sqrt{\frac{\alpha}{\mathrm{E\{A_i^2\}}}} \tag{3}$$

where K_n is the modified Bessel function of second kind of order n, $E\{A_i^2\}$ the second moment of the amplitude, and α the effective number of scatterers per resolution cell or the effective density of scatterers.

B. Experimental Checking of Distributions

Since scatterer density and distribution within biological tissues are not known features, we have investigated independently the envelope statistics of the blood and that of arterial wall echoes in our images. The study consists of selecting, within ultrasound envelope images, regions of homogeneous brightness, computing their histograms and comparing them with the above probability density functions. We have observed that, in most of cases, the echo envelope brightness follows a Rayleigh distribution or a K-distribution, but with a large scatterer density that makes it similar to the Rayleigh distribution [Fig. 1(a)]. Only a few cases were found to follow a K-distribution, distinct from that of Rayleigh [Fig. 1(b)].

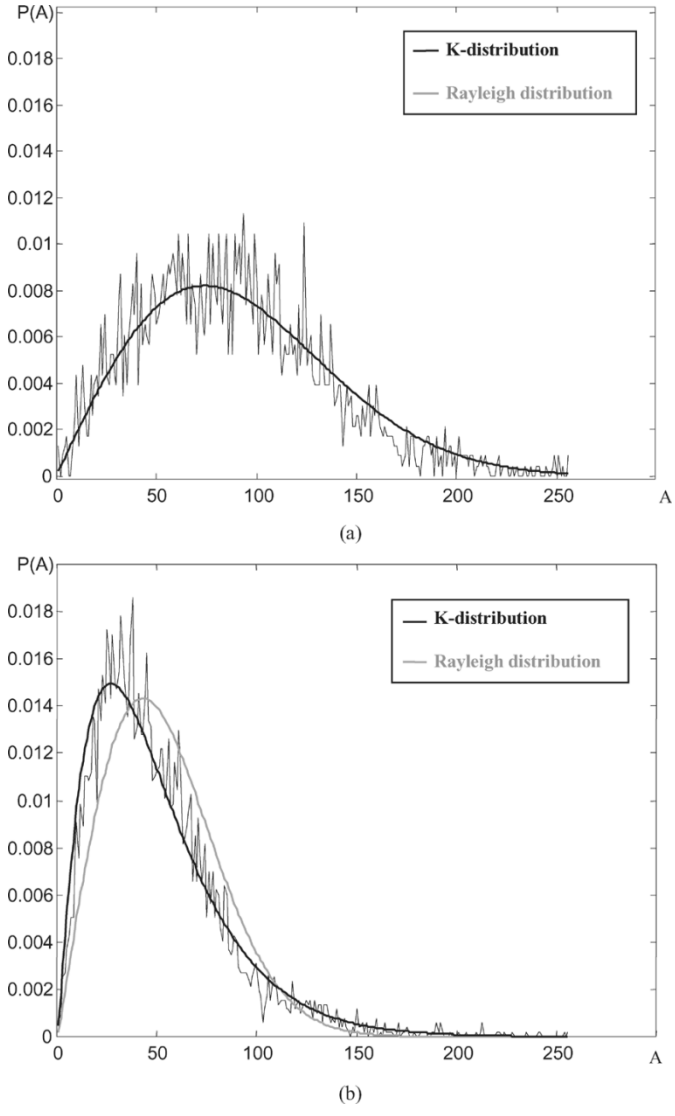

Fig. 1. Illustration of the echo envelope brightness statistics in the images under investigation. (a) The pixel amplitude follows a Rayleigh distribution, or a K-distribution, but with a scatterer density sufficiently large to allow no distinction between the two curves. This corresponds to the majority of cases. (b) The pixel amplitude here follows a K-distribution, distinct from the Rayleigh distribution. This has been observed in a few cases only.

Since the K-distribution is a generalization of the Rayleigh distribution, these observations would suggest the use of the former as a model of the pixel amplitude in our images. However, some additional considerations have to be taken into account and, in particular, the accuracy of the distribution parameter estimates. Several techniques have been proposed to estimate distribution parameters. The maximum likelihood method has the least variance of all the parameter estimation techniques and is preferred whenever it can be used. This method is employed when sample sizes are small but the form of distribution is known. It employs a likelihood function which computes the probability that the observed samples come from a distribution with specified parameters. The parameter estimates are, therefore, the values that maximize the likelihood function. For

probability density functions like the Rayleigh model, the likelihood function results in a closed-form expression and parameter estimates can, thus, be easily computed [32], [33]. But for the case of K-distributions, a closed-form solution to the likelihood function is unobtainable [41]. A numerical approximation to this function can be adopted at a high computational cost, or parameters can be estimated using a moment method [41], [49]. The problem with moment methods is that they require large sample sizes to estimate the sample moments with small enough variance to provide parameter estimation with a reasonable precision. This condition is unfortunately hardly met.

For all these reasons, we chose to approximate the ultrasound envelope image brightness by Rayleigh distributions, for which parameter estimates can be accurately and quickly computed.

C. Bayesian Estimation of the Endoluminal Contour Position

Let us consider an IVUS B-mode image I. The searched contour (denoted by C) is the border between the blood (*Rb*) and the arterial wall (*Rw*). By using the Rayleigh model for the image brightness, the contour position can be statistically estimated. It is searched as a continuous, smooth closed curve that optimally separates two Rayleigh distributions, one modeling the blood brightness and identified by the parameter α_{b}, the other characterizing the arterial wall brightness and identified by α_{w}.

A suitable statistical procedure to determine the contour position from an initial *a priori* contour C with prior probability $\mathrm{P(C)}$, is the Bayesian estimation [32], [33], [37]. The Bayesian estimator that is often used in practice is the maximum *a posteriori* (MAP) approach. The *a posteriori* probability $\mathrm{P(C|I)}$ computes for a given contour position its probability to occur. By considering all possible positions for the contour C, and given the image I, $\mathrm{P(C|I)}$ can be seen as a function, that gives the *a posteriori* probability as a function of C. The MAP approach, thus, searched the contour as the argument that maximizes $\mathrm{P(C|I)}$, i.e., that has the highest probability to occur, for the image I.

This approach performs well when two regions have to be discriminated. For the present vascular application, this technique will accurately detect the border between the blood and the tissue, provided that both have a homogeneous brightness. This condition is unfortunately rarely met. Indeed, the arterial wall, specifically in the presence of an atherosclerotic plaque, is highly heterogeneous. This implies that the representation of the arterial wall in ultrasound images is not a single wide area, but several juxtaposed regions whose brightness follows different Rayleigh statistics. This complicates the shape of the function $\mathrm{P(C|I)}$. We will show in the following developments that this implies that the searched border does not necessarily correspond any more to the position of the function maximum, but rather to a local maximum. For those reasons we propose an approach that combines the information of both the global and local maxima of the *a posteriori* probability $\mathrm{P(C|I)}$.

By Bayes' rule, the function of interest $\mathrm{P(C|I)}$ can be expressed as

$$\mathrm{P(C\,|I)} = \frac{\mathrm{P(I\,|C)P(C)}}{\mathrm{P(I)}} \tag{4}$$

where $\mathrm{P(I|C)}$ is the data model and $\mathrm{P(I)}$ is the *a priori* data probability, a normalization constant which only depends on the noise. For expression simplification and computation time gain purposes, the equivalent formulation (5) is preferred. This is made possible since the logarithm is a strictly increasing function, thus conserving the global and local maxima location

$$\ln\big[\mathrm{P(C\,|I)}\big] = \big[\ln[\mathrm{P(I\,|C)}] + \ln[\mathrm{P(C)}] - \ln[\mathrm{P(I)}]\big]. \tag{5}$$

In our study, the data statistical model $\mathrm{P(I|C)}$ is based on Rayleigh distributions. Since two independent regions are considered, the blood and the arterial wall, the analytical expression of $\mathrm{P(I|C)}$ is

$$\begin{aligned}\mathrm{P(I\,|C)} &= \prod_{\mathrm{i}\in\mathrm{Rb}} \mathrm{P(A_i\,|C)} \prod_{\mathrm{j}\in\mathrm{Rw}} \mathrm{P(A_j\,|C)} \\ P(\mathrm{I\,|C}) &= \prod_{\mathrm{i}\in\mathrm{Rb}} \frac{\mathrm{A_i}}{\alpha_{\mathrm{b}}^2(\mathrm{C})} \exp\left(-\frac{\mathrm{A_i^2}}{2\alpha_{\mathrm{b}}^2(\mathrm{C})}\right) \\ &\quad \times \prod_{\mathrm{j}\in\mathrm{Rw}} \frac{\mathrm{A_j}}{\alpha_{\mathrm{w}}^2(\mathrm{C})} \exp\left(-\frac{\mathrm{A_j^2}}{2\alpha_{\mathrm{w}}^2(\mathrm{C})}\right)\end{aligned} \tag{6}$$

where $\mathrm{A_i}$ is the brightness value of the $\mathrm{i^{th}}$ sample, and $\alpha_{\mathrm{b}}(\mathrm{C})$ and $\alpha_{\mathrm{w}}(\mathrm{C})$ are the parameters of the probability density functions, depending on the contour position, and on the brightness of regions *Rb* and *Rw*, respectively. Combining (6) and (5) leads to

$$\begin{aligned}\ln(\mathrm{P(C\mid I)}) = \Bigg[&- \sum_{\mathrm{i}\in\mathrm{Rb}} \ln(\alpha_{\mathrm{b}}^2(\mathrm{C})) - \sum_{\mathrm{j}\in\mathrm{Rw}} \ln(\alpha_{\mathrm{w}}^2(\mathrm{C})) \\ &- \frac{1}{2}\sum_{\mathrm{i}\in\mathrm{Rb}} \frac{\mathrm{A_i^2}}{\alpha_{\mathrm{b}}^2(\mathrm{C})} - \frac{1}{2}\sum_{\mathrm{j}\in\mathrm{Rw}} \frac{\mathrm{A_j^2}}{\alpha_{\mathrm{w}}^2(\mathrm{C})} + \sum_{\mathrm{i}\in\mathrm{Rb}} \ln(\mathrm{A_i}) \\ &+ \sum_{\mathrm{j}\in\mathrm{Rw}} \ln(\mathrm{A_j}) + \ln(\mathrm{P(C)}) - \ln(\mathrm{P(I)})\Bigg]\end{aligned} \tag{7}$$

with $\sum_{\mathrm{i}\in\mathrm{Rb}}\ln(\mathrm{A_i}) + \sum_{\mathrm{j}\in\mathrm{Rw}}\ln(\mathrm{A_j}) = \sum_{\mathrm{k}\in\mathrm{I}}\ln(\mathrm{A_k}) = \mathrm{constant} = \mathrm{k}$ since $\mathrm{I} = \mathrm{Rb} \cup \mathrm{Rw}$

The last requirement is the estimation of the parameters α_{b} and α_{w} of the Rayleigh distributions. These unknown parameters are estimated with the maximum likelihood approach. The principle is to find the parameter value of the Rayleigh distribution that would have most likely produced the data we observe. The procedure consists in computing the likelihood function. The searched parameter value is the one that makes the likelihood function reaches its maximum. This function, denoted by L, is the joint probability function of the considered samples and is defined for the estimation of the parameter α_{b} by

$$\mathrm{L(A_1,\ldots,A_{\mathit{n}}\,|}\alpha_{\mathrm{b}}) = \prod_{\mathrm{i}=1}^{n} \mathrm{P(A_i\,|}\alpha_{\mathrm{b}}) \tag{8}$$

where n is the number of considered observations, which is in our case the number of samples of region *Rb*.

For the purpose of simplification, using the logarithm of the likelihood function is preferred, since that transforms the problem of maximizing a product into maximizing a sum. Thus, the optimal value for α_{b} is the solution of

$$\frac{\mathrm{d}(\ln \mathrm{L(A_1,\ldots,A_{\mathit{n}}\,|}\alpha_{\mathrm{b}})}{\mathrm{d}\alpha_{\mathrm{b}}} = 0 \tag{9}$$

leading to

$$\alpha_{\mathrm{b}}(\mathrm{C}) = \sqrt{\frac{1}{2\mathrm{n_b(C)}} \sum_{\mathrm{i}\in\mathrm{Rb}} \mathrm{A_i^2}} \tag{10}$$

where $n_{\mathrm{b}}(C)$ is the number of samples in region *Rb*, given C.

Similarly, the maximum likelihood estimator for α_{w} is

$$\alpha_{\mathrm{w}}(\mathrm{C}) = \sqrt{\frac{1}{2\mathrm{n_w(C)}} \sum_{\mathrm{j}\in\mathrm{Rw}} \mathrm{A_j^2}} \tag{11}$$

with $n_{\mathrm{w}}(C)$, the number of samples in region R_{w}, given C.

By replacing $\alpha_{\mathrm{b}}(C)$ and $\alpha_{\mathrm{w}}(C)$ by their estimates in (7), the expression of $\ln[\mathrm{P(C|I)}]$ becomes

$$\ln(\mathrm{P(C\,|\,I)}) = \big[-\mathrm{n_b(C)}\ln(\alpha_{\mathrm{b}}^2(\mathrm{C})) - \mathrm{n_w(C)}\ln(\alpha_{\mathrm{w}}^2(\mathrm{C})) - (\mathrm{n_b(C)} + \mathrm{n_w(C)}) + \ln\mathrm{P(C)} - \ln(\mathrm{P(I)}) + \mathrm{k}\big]. \tag{12}$$

The contour model $\mathrm{P(C)}$ can take many different forms (set of points, parametric contour, …). The model implemented in our algorithm will be fully described in the next section.

As previously mentioned, the searched borders may correspond not only to the global maximum but also to a local maximum of $\mathrm{P(C|I)}$ and, thus, of $\ln(\mathrm{P(C|I)})$. In order to illustrate these difficulties, we have simulated three 3-layer media and computed the corresponding functions $\mathrm{P(C|I)}$ (Figs. 2 and 3). The first simulated medium is composed of 3 layers (*l1*,*l2*,*l3*) of equal size L [Fig. 2(a)]. Within each layer, the pixel amplitude has been generated with a Rayleigh distribution [Fig. 2(b)]. The only difference results from the distribution parameter value α^2 that has been set to 25 for *l1*, to 60 for *l2* and to 300 for *l3*. The second medium has identical statistical properties than those of the medium 1, except that the layers *l2* and *l3* have been reversed. The third medium is also the same as the first one, except that the first layer has been shortened [Fig. 2(a)]. These simulations are good representations of IVUS images we have to work with. Let us consider the darker area *l1* as the blood and *{l2,l3}* as the tissue. The first simulation is representative of the brightness heterogeneity of the arterial wall, due to the attenuation of the ultrasound beam with depth [51], [52]. The brightness of the deeper layer *l3* is, thus, darker than that of the layer *l2*. The second medium is a good representation of images of arteries with soft plaques (which would correspond to *l2*). Indeed soft plaques are mostly hypo-echoic, with a brightness that is slightly higher than that of the blood. Finally, the third simulation is representative of the situation where the catheter is positioned close to the arterial wall, which leads to a small blood area.

For these three configurations the functions $\mathrm{P(C|I)}$ were computed. The *a priori* information on the layer interfaces is that they are vertical edges. $\mathrm{P(C|I)}$ is, thus, determined by moving a virtual vertical border from left to right, and by computing the a *posteriori* probability for each position. Results are presented in Fig. 3. We observe that the shape of the function depends on the number of regions, their sizes, and the brightness contrast between regions. The searched border, which in our simulations is the boundary between *l1* and *l2*, rarely corresponds to the global maximum of the function $\mathrm{P(C|I)}$, but generally to a local maximum. The explanation is simple: because in the medium 2 the brightness contrast is low between *l1* and *l2*, and strong between *l2* and *l3*, separating this medium into two regions implicitly leads to the result that *l1* and *l2* belong to the same part. The maximum of the *a posteriori* probability is, thus, reached at the higher contrast interface. Similarly, because in medium 3 the size of the first layer is small and because the contrast between *l2* and *l3* is high, dividing this medium into two areas implicitly leads to the result that the most probable border is the one between *l2* and *l3*. However, whatever the case, the borders correspond to either global or local maxima of the function $\mathrm{P(C|I)}$ and are highlighted in the function derivative.

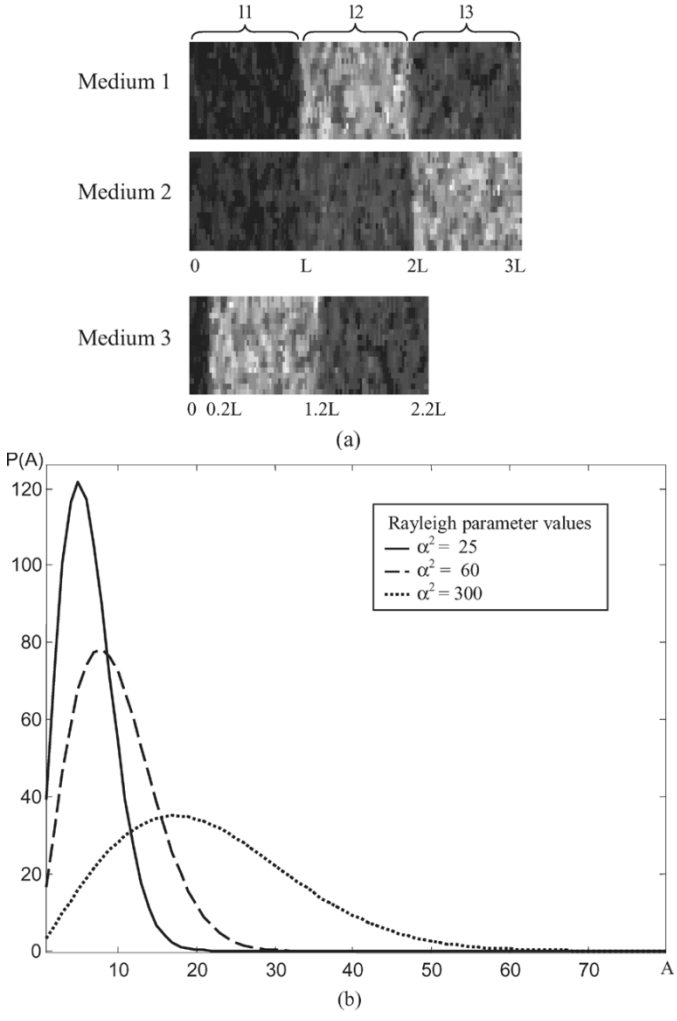

Fig. 2. (a, b) Illustrative simulations. The medium 1 is composed of 3 layers (*l1*, *l2*, *l3*) of equal size L. Within each layer, the pixel amplitude follows a Rayleigh distribution, with a parameter value α^2 set to 25 for *l1*, to 60 for *l2*, and to 300 for *l3* (b). The medium 2 has identical statistical properties than those of the medium 1, excepted that the layers *l2* and *l3* have been reversed. The medium 3 is identical to the medium 1, but with a shorter first layer.

Contour position estimation using both the global (13) and local maxima (14) of $\mathrm{P(C|I)}$ will be considered in the following developments:

$$\widetilde{\mathrm{C}} = \arg\max_{\mathrm{C}} \big[-\mathrm{n_b(C)}\ln(\alpha_{\mathrm{b}}^2(\mathrm{C})) - \mathrm{n_w(C)}\ln(\alpha_{\mathrm{w}}^2(\mathrm{C})) + \ln\mathrm{P(C)}\big] \tag{13}$$

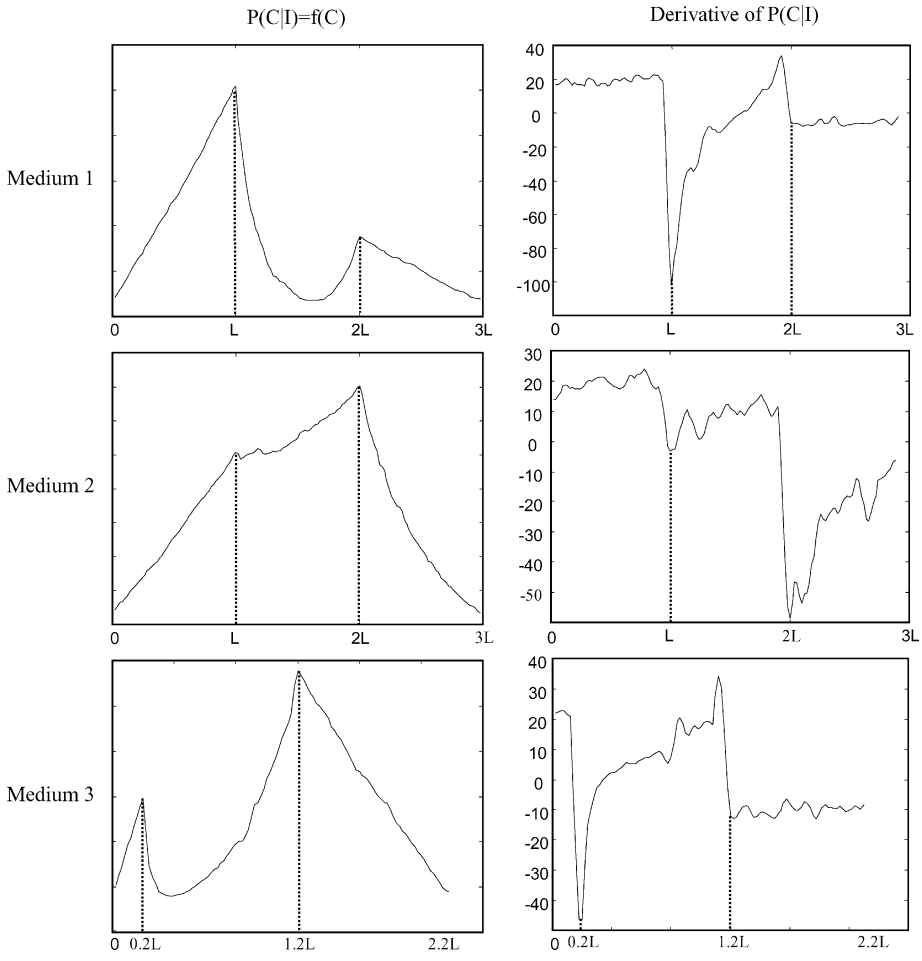

Fig. 3. Representation of the *a posteriori* probability $\mathrm{P(C|I)}$ and its derivative, as a function of the contour position C. We can observed, that the searched border corresponds to either global or local maximum of $\mathrm{P(C|I)}$. This observation is put in relief in the function derivative.

having removed the terms whose summation yields a constant, since they do not intervene in the maximization problem, and

$$\frac{\mathrm{d}[\ln(\mathrm{PC|I})]}{\mathrm{dC}} = 0. \tag{14}$$

It should be noted that the previously discussed methods only used the *maximum a posteriori* estimator.

III. Method Implementation

The major interest of our method for the blood-wall interface segmentation in IVUS images is that it is fully automatic. Indeed, it does not require that the user preselects an ROI tight around the lumen boundary, or chooses a set of parameter values. This fully automatic characteristic is achieved by one essential feature of the method: contrary to most classical snake-based algorithms, the initial contour position is computed from the information of both the function $\mathrm{P(C|I)}$ and its derivative.

The implementation of our segmentation method includes the three main following steps:

1) preprocessing;
2) initial contour computation;
3) contour evolution.

All of them are performed on polar images. The raw data, used in this study, are RF intracoronary ultrasound images. These RF data were acquired *in vivo* with a JOMED Invision ultrasound scanner, working with a 20-MHz 64-element array catheter.

A. Step 1) Preprocessing

Acquired images frequently have a poor SNR and/or a low blood-to-tissue ratio. Moreover they are affected by the presence of a "ring-down artifact" (Fig. 4). This artifact is nearly time invariant, and caused by the physical features of the catheter. It results in a high brightness region around the catheter, which makes it difficult to detect the blood-tissue interface close to the probe.

To facilitate border segmentation, three preprocessing steps are applied to improve the image quality. These steps are an image truncation, a ring-down artifact amplitude weakening and a detection of the signal envelope.

1) Image Truncation: The basis of our algorithm is to make a snake evolve until it separates two regions, the blood and the tissue. In IVUS images, we can observe three regions: the blood, the arterial wall, and an area corresponding to the dead zone of the catheter (Fig. 4). The latter, of catheter size, contains no information about the blood or the tissue, and needs to be removed, otherwise it will negatively influence the evolution of

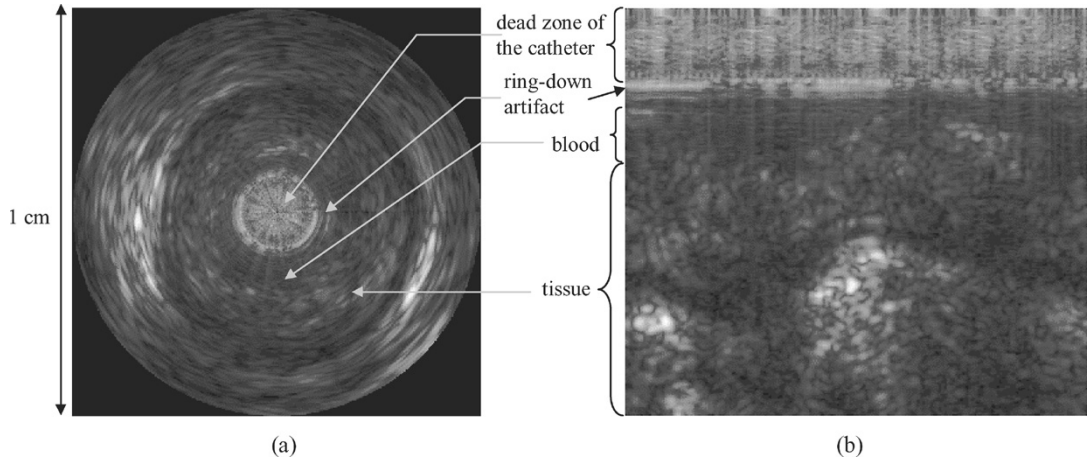

Fig. 4. Typical B-mode image to process (a) in Cartesian coordinates and (b) in polar coordinates. We can observe the blood, the tissue, the dead zone of the catheter, and the ring-down artifact.

the active contour. This operation is easy to perform since the catheter, as the imaging element, is always located at the image center (in Cartesian coordinates), which corresponds to the first lines in range of the image (in polar coordinates). In practical terms, the number of lines corresponding to the catheter radius are automatically removed from the polar image.

2) Ring-Down Artifact Amplitude Weakening: The ring-down artifact has the property of being nearly invariant in time. Averaging successive RF frames, thus, preserves the artifact amplitude while strongly decreasing the amplitude of the other structures. An averaged image of the ring-down artifact can, therefore, be computed. The removal of this artifact is achieved by subtracting the artifact averaged image from the image under investigation (15).

$$\mathrm{I_{filt}}(\mathrm{r},\theta) = \mathrm{I_{ini}}(\mathrm{r},\theta) - \frac{1}{\mathrm{Nb}}\sum_{\mathrm{k}=1}^{\mathrm{Nb}} \mathrm{I_k}(\mathrm{r},\theta) \tag{15}$$

where

I_{ini} initial RF image, characterized by the presence of the ring-down artifact;
I_{k} raw RF images;
Nb number of RF images used for the averaging;
I_{filt} resulting filtered RF image.

The number of images Nb used for the averaging has been fixed to 50. This number has been observed to be sufficient to ensure an artifact averaged image of good quality.

3) Envelope Detection: The enveloped detected image is then computed as the absolute value of the Hilbert transform of the artifact filtered RF image. The resulting envelope polar image will be denoted $I(r,\theta)$ from now on.

It has to be underlined that resulting image brightness statistics are in agreement with the theory (Section II-A). Indeed the experimental checking of the image brightness distributions presented in Section II-B was performed after these preprocessing steps.

B. Step 2) Initial Contour Computation

Contrary to classical snake-based algorithms, our method involves computing the initial contour. Let us divide the envelope polar image $I(r,\theta)$ into N regions of equal width along the angular direction. These regions are denoted by R_{i}, $i \in [1,\ldots,N]$ (Fig. 5). To each region we attribute a point of the contour, M_{i}. Hence, the contour (C) is a polygon with N control points. These points are regularly positioned along the angular direction in the middle of each region R_{i}. Only their position in the radial dimension, r_{i}, remains to be determined. This leads to a representation of the contour as a one-dimensional vector

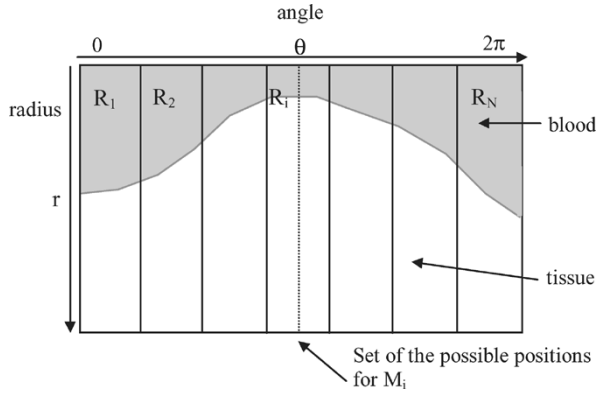

Fig. 5. Problem representation. The polar image under investigation is divided into N regions of equal width ($R_{\mathrm{i}}, i \in [1,\ldots,N]$) along the angular direction. To each region R_{i}, is attributed a point M_{i} of the contour. The contour C is, thus, searched as a polygon with N control points. The angular position of M_{i} corresponds to the middle of R_{i}. Only its radial position r_{i}, remains to be determined.

$$\mathrm{C} = \left\{ \mathrm{M_i}\left(\mathrm{r_i}, \theta_{\mathrm{i}} = (\mathrm{i}-0.5)\cdot\frac{2\pi}{\mathrm{N}}\right),\ \mathrm{i}\in[1..\mathrm{N}] \right\}. \tag{16}$$

For each M_{i}, the computation of its radial position r_{i} is performed independently of the other points. It integrates information from the maximum of the function $\mathrm{P(C|I)}$ (i.e., the MAP estimator) and its derivative. Because the width of R_{i} is small, we assume that, over this region, the border between the blood and the tissue is a horizontal straight line. Therefore $\mathrm{P(C|I)}$ is computed at all the radial positions of this line. The assumption that the blood-wall interface is a horizontal line is only used for the computation of $\mathrm{P(C|I)}$. The initial contour will be obviously the union of the N points M_{i}.

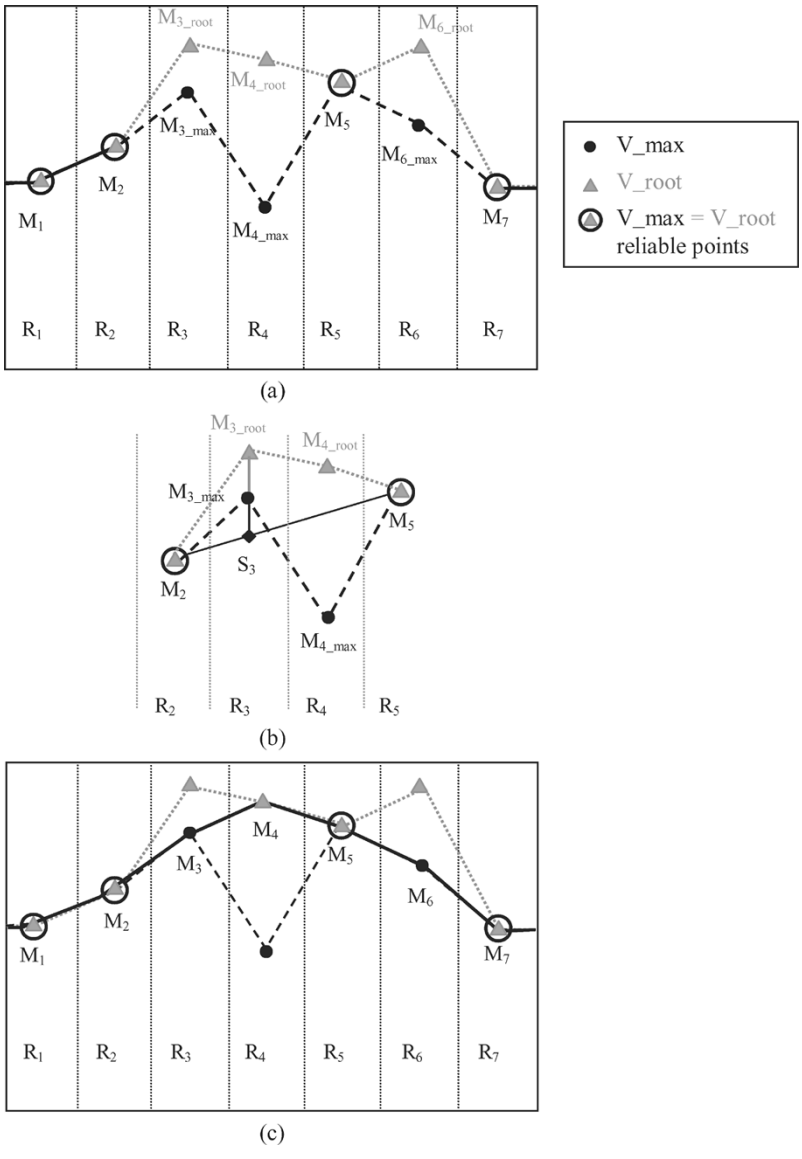

Fig. 6. Illustration of the initial contour computation with $N = 7$ (a) Determination of the reliable points, for which the maximum of the function $\mathrm{P(C|I)}$ is at the same radial position than the first zero crossing of its derivative ($r\_\max = r\_root$) (b) Determination of the initial contour between two reliable points. It is searched as the shortest path through $r\_\max$ and r_root to join the two considered reliable points (c) resulting initial contour.

The location of the function maximum is then determined, as well as the first zero crossing of the derivative. This information is saved in two vectors $r\_\max$ and r_root, of length N, which give for each point M_i its two possible radial positions $r\_\max(i)$ and $r\_root(i)$. We emphasize that among the zero-crossings of the derivative, only the first one is here considered. Indeed in IVUS images, brightness heterogeneity occurs mainly in the arterial wall, whereas blood brightness is more homogeneous. Under these conditions, the luminal border has to be searched as the *first zero-crossing* of the function derivative. However, the ring-down artifact weakening step modifies locally the blood statistical properties. Over sectors where the artifact is concentrated, this preprocessing significantly modified the brightness statistics. As a result, the first zero-crossing no longer corresponds to the luminal border. This is why is also necessary to consider both the first zero-crossing of the derivative as well as the MAP estimator.

The initial contour is determined in two steps, as illustrated in Fig. 6 (with $\mathrm{N} = 7$).

1) First, the points for which the maximum of the function $\mathrm{P(C|I)}$ and the first zero-crossing of its derivative are at the same radial position, have a strong probability to be well located. They are points selected for the initial contour, and are termed *reliable points*. In our example, they correspond to M_1, M_2, M_5, and M_7.
2) Then, for the points for which the maximum of the function $\mathrm{P(C|I)}$ is at a different position than that of the first zero-crossing of the derivative, both radial positions $r\_\max(i)$ and $r\_root(i)$ are considered as possible. Let us denote by $M_{\mathrm{i\_max}}$ ($M_{\mathrm{i\_root}}$, respectively) the point whose coordinates are $(r\_\max(i), \theta_\mathrm{i})$ $(r\_root(i), \theta_\mathrm{i})$, respectively). We have to select which one of the two points $M_{\mathrm{i\_max}}$ and $M_{\mathrm{i\_root}}$ is going to be used for the contour initialization. This selection requires consideration of the two nearest reliable points on

both sides of θ_i [Fig. 6(b)]. Let us consider the region R_3, where M_{3_max} and M_{3_root} are two distinct points. The two nearest reliable points on both sides of θ_3 are M_2 and M_5, respectively. The segment $[M_2M_5]$ represents the absolute shortest path between the two points. Let S_3 be the point of $[M_2M_5]$, at angular position θ_3. S_3 is, thus, the point of reference with respect to the shortest path problem. Between M_{3_max} and M_{3_root}, the one chosen for the contour initialization is the one closer to S_3 [M_{3_max}. in our example, Fig. 6(c)].

To sum up, the initial contour is obtained by first determining all the reliable points, and by then finding the shortest path through $r\_\max$ and r_root to join two reliable points.

It has to be specified that the situation for which no reliable points would have been found, has never been encountered. On average around half of the points that compose an initial contour have been determined as reliable points. Then, by completing the contour with the shortest path strategy, we have observed that, in most of the cases, the initial contour is already close to its final position.

C. Step 3) Contour Evolution

The contour evolution process is no longer performed over the entire image but rather in an ROI around the contour. This ROI ranges from x pixels above the contour to x pixels below it and will evolve with the contour.

At this step of the segmentation, *a priori* information about the contour is introduced, to ensure that the final curve is smooth and closed. The contour model $\mathrm{P(C)}$ expresses for each contour point a strong correlation with its close neighbors and neglects the influence of the other contour points further apart. To limit computational requirements, we have, for each contour point, taken into account the influence of the two adjacent neighbor positions only (17). This has been observed to be sufficient (see results Section IV)

$$\mathrm{P(C)} = \exp\left\lfloor \lambda \left((\mathrm{r_i} - \mathrm{r_{i-1}})^2 + (\mathrm{r_i} - \mathrm{r_{i+1}})^2 \right) \right\rfloor \qquad (17)$$

where λ is the smoothness constraint. Large values of λ imply smoother contours.

Hence, starting from the initial contour, the contour evolves according to the scheme of iteratively defining the ROI and computing the new contour position. This process stops when the contour motion becomes so small that it can be ignored. The statistical criteria we compute for estimating the new contour position is the MAP estimator only. Indeed because the size of the ROI is limited, the maximum of the function $\mathrm{P(C|I)}$ and the first zero crossing of its derivative occur at the same radial position nearly all the time. Since it requires less computational effort, the MAP estimator (13) was preferred.

D. Extension

The algorithm can be used to process image sequences. Two images, consecutive in time or in space, often exhibit strong similarities, and corresponding luminal contours are close to one another. Using the final contour in the image [i] as the initial contour for the image [i + 1] is not only suitable, but facilitates and accelerates the convergence of the snake to the searched contour, since only the contour evolution step remains to be performed.

IV. Results

In vivo coronary images from 15 patients, acquired with a 20-MHz central frequency JOMED Invision ultrasound scanner, were segmented with the developed method. Images with a very low SNR, soft plaques and stents were included in this study. Only the situations of totally occlusive plaques, dissections and side-branches were ignored. All the images were processed with the same parameter values which were: the number of contour points N set to 26, the smoothness constraint λ fixed to 0.5 and the ROI size parameter x initialized to 30. The number of contour points was chosen high enough to follow accurately any luminal shape, and low enough to limit computation time. The smoothness constraint λ was determined heuristically, allowing for variations between contour points while annihilating discontinuities.

Six segmented contours are displayed in Fig. 7 to illustrate the border detection performance. Several illustrations of an eccentric catheter close to the arterial wall are presented [Fig. 7(a)–(e)]. We can observe that the algorithm converges to the right contour even when the catheter is close to a soft hypoechoic plaque [Fig. 7(a)]. Similarly, in the case of a very narrow lumen [Fig. 7(f)] the small size blood area has not prevented the algorithm to detect the luminal border. Finally, in Fig. 7(c), the image of a coronary artery with a stent restenose is displayed. The stent is not located on the surface of the arterial wall but inside the wall. Its representation in the B-mode image is a set of highly bright spots, that can negatively influence the contour detection. However, the snake has not been attracted by the bright spots and the detected contour is the correct interface.

To assess the performance of the presented technique, the automatic contours were compared to those manually traced by two experienced physicians. Manual contours are represented by a variable number of irregularly spaced points. To enable comparison between two contours, it is fundamental that each point of one contour has a corresponding point in the other. This problem was overcome by interpolating the contours along the angular direction.

For each frame, the mean radius from manually traced and automatically detected lumen contours were compared (Fig. 8). Results demonstrate a high correlation (regression line: $\mathrm{y} = 0.93\mathrm{x} + 0.05$, correlation coefficient $\mathrm{r} > 0.97$, $\mathrm{p} < 0.001$), although we observed that the algorithm slightly underestimated the contours in comparison to physicians. To assess the position of automatic contours, two kinds of errors were computed: the error between the automatic contours and the average of the manual ones, (Err) as described in (18), and the error between the manual contours (Err_expert). Results are reported in Table I. The error between two contours is defined as the mean absolute difference on the radial position of the contour points

$$\mathrm{Err} = \frac{1}{\mathrm{Np}} \sum_{\mathrm{i}=1}^{\mathrm{Np}} \left| \mathrm{r_{i\_automatic}} - \mathrm{r_{i\_drawn\_averaged}} \right| \qquad (18)$$

where Np is the number of points, considered for the error computation.

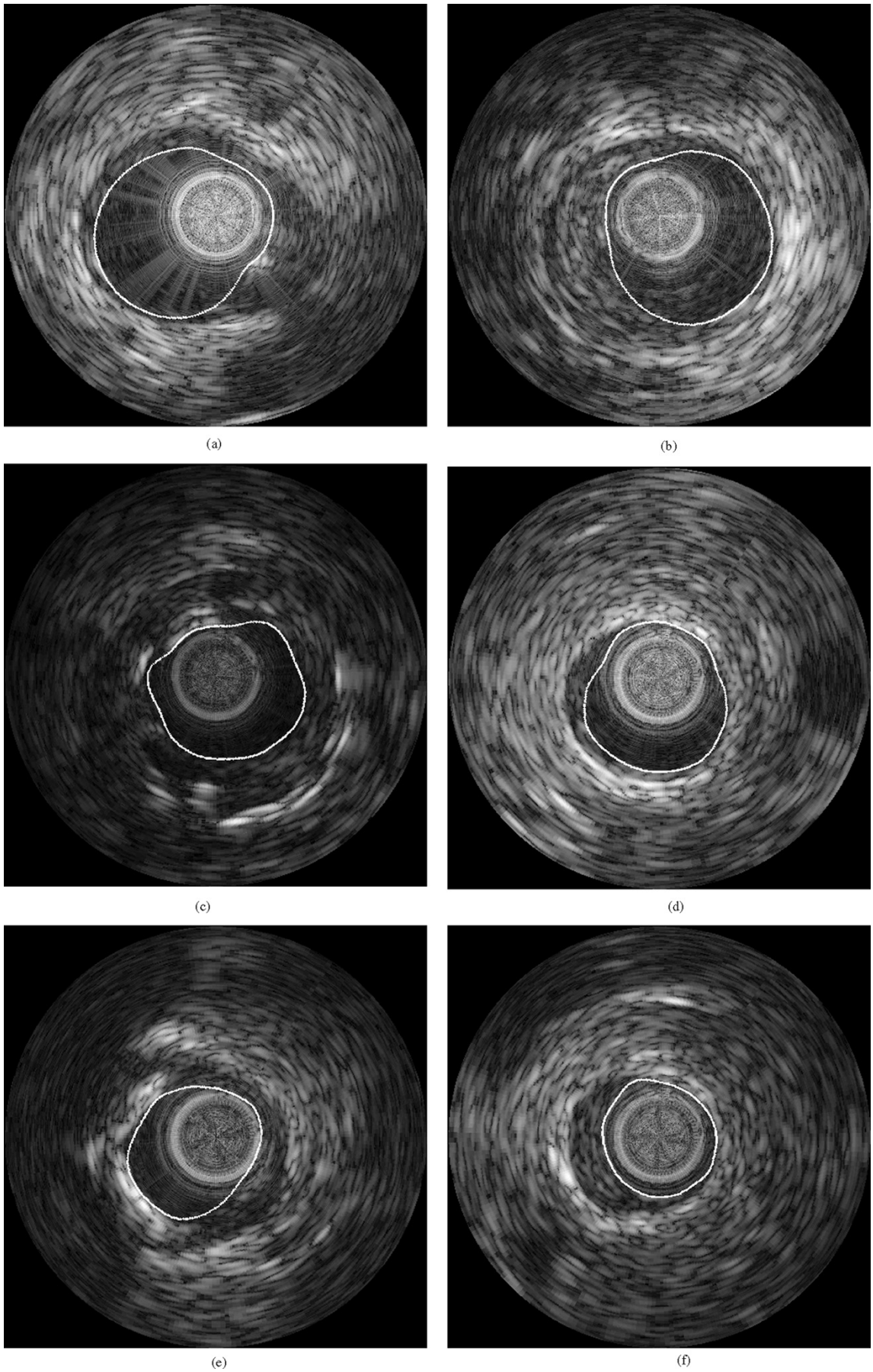

Fig. 7. Six examples of automatically computed contours, including the cases of (a)–(e) an eccentric catheter position close to the arterial wall, (c) a stent restenose, and (f) a narrow lumen. In all cases the active contour converges to the searched luminal border.

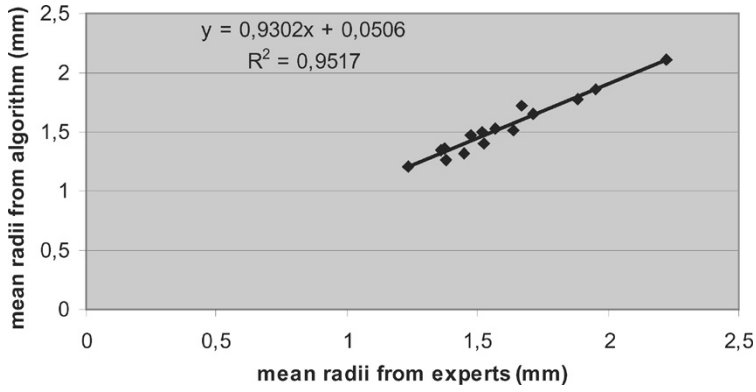

Fig. 8. Correspondence of the mean radii of luminal contours determined by the algorithm and measured by the experts.

TABLE I
PERFORMANCE EVALUATION OF THE FULLY AUTOMATIC SEGMENTATION. MEAN, STANDARD DEVIATION, MINIMUM, AND MAXIMUM OF THE MEAN ABSOLUTE DIFFERENCE IN RADIUS BETWEEN TWO EXPERTS (EXPERT ERROR) AND BETWEEN THE COMPUTED CONTOURS AND THE EXPERTISE (EXPERT VERSUS ALGORITHM ERROR) ARE SUMMARIZED. THE DIFFERENCE BETWEEN A CONTOUR OBTAINED BY THE ENTIRE PROCESSING FOR AN IMAGE [i + 1] AND THE CORRESPONDING ONE COMPUTED BY USING AS INITIAL CONTOUR THE FINAL CONTOUR FOR THE IMAGE [i] HAS ALSO BEEN INVESTIGATED (EXTENSION ERROR)

	Inter-expert error (*Err_expert*)	Experts vs algorithm error (*Err*)	Extension error (*Err_extension*)
Mean ± SD (mm)	0.097 ± 0.027	0.099 ± 0.032	0.015 ± 0.013
Minimum (mm)	0.05	0.04	0.0005
Maximum (mm)	0.15	0.15	0.037

TABLE II
PERFORMANCE EVALUATION OF THE FULLY AUTOMATIC SEGMENTATION. MEAN, STANDARD DEVIATION, MINIMUM, AND MAXIMUM OF THE MEAN ABSOLUTE AND RELATIVE DIFFERENCES IN AREAS BETWEEN TWO EXPERTS (EXPERT ERROR) AND BETWEEN THE COMPUTED CONTOURS AND THE EXPERTISE (EXPERT VERSUS ALGORITHM ERROR) ARE SUMMARIZED. RESULTS FOR THE ALGORITHM 3-D EXTENSION ARE ALSO REPORTED

	Inter-expert error		Experts vs algorithm error		Extension error	
	Area (mm²)	Area (%)	Area (mm²)	Area (%)	Area (mm²)	Area (%)
Mean ± SD	0.47 ± 0.40	6.3 ± 5.8	0.70 ± 0.48	8.2 ± 5.4	0.16 ± 0.15	2.1 ± 2.2
Minimum	0.0073	0.08	0.028	0.42	0.005	0.09
Maximum	1.36	19.8	1.5	16.7	0.50	7.5

The results of the comparison of contours drawn by two experts are the following. The interexpert error, Err_expert, has been estimated to 0.097 ± 0.027 mm. This means that the mean absolute error on the radial position of the contour points is equal to 0.097 mm. The corresponding value for the error between the automatic contours and the average of the manual ones has also been determined. It has been found equal to 0.099 ± 0.032 mm, i.e., only slightly higher than the interexpert error. The maximal value of Err has been estimated to be 0.15 mm. This is identical to the maximal error between experts. Finally, the minimal radial position error of the algorithm versus experts (0.04 mm) is inferior to that between experts (0.05 mm).

The comparative study dealt also with the absolute and relative differences of the corresponding areas (Table II). Because manual contours remain the reference, the algorithm versus expert area relative difference was computed as the absolute difference related to the experts. For the expert area relative difference, we have considered as a reference the average of the two manual areas drawn by the physicians. This interexpert relative difference has, thus, been computed as the absolute difference between the two manual areas related to their average. Results are the following: the mean absolute (relative) difference between manually determined areas has been estimated to 0.47 ± 0.4 mm^2 ($6.3 \pm 5.8\%$, respectively). Between automatic areas and the average of the manual ones, the absolute and relative differences have been found equal to 0.70 ± 0.48 mm^2 and $8.2 \pm 5.4\%$, respectively. These values are only a little bit higher than the expert errors. The maximum area difference between experts (1.36 mm^2) and between experts and the algorithm (1.5 mm^2) are of the same order.

These results demonstrate a good correlation between the computed contours and those manually drawn by the two physicians.

A first evaluation on the method extension was also performed. We investigated the behavior of the algorithm to process image sequences. The final contour for an image [i] was used as the initial contour for the image [i + 1]. Thus only the contour evolution step needed to be performed. In order to quantify the influence of this contour initialization, the resulting final contours were compared to those obtained by the entire processing. The corresponding error is termed extension_error in Table I. We observe that, the resulting contours are very close to those obtained by the entire processing. Indeed, the mean absolute error on the contour radial position was estimated to 0.015 ± 0.013 mm, which is very inferior to

the interexpert error. The maximal *extension_error* has been found to 0.037 mm. It still remains significantly lower than the mean interexpert error. These results are corroborated by those obtained for the corresponding areas. Only slight differences are observed, that have a global tendency of slightly improving the contour position.

V. Conclusion and Discussion

In this paper, a fully automatic algorithm, dedicated to luminal contour segmentation in IVUS images has been introduced. The technique is based on an active contour that evolves according to the image statistical properties. The analysis of the echo envelope statistics of the images we work with, has led us to model the B-mode image brightness by Rayleigh distributions. The idea is then to make the contour evolve, until it separates the blood and the tissue, represented by different Rayleigh distributions. The main interest of the algorithm presented in this paper is that it requires *no user intervention*. The fully automatic character has been achieved by computing a good guessed initial contour, from two pieces of information extracted from $\mathrm{P(C|I)}$. They are the location of the function maximum (MAP estimator) and of the first zero-crossing of the derivative. Previously reported works only make use of the *MAP* estimator to perform segmentation.

The method evaluation was performed in comparison to contours drawn by two experts. Results have demonstrated that the error between the computed contours and the average of the manual ones is of very small amplitude (0.099 mm), and of the same order than the interexpert error (0.097 mm)

The 3-D extension of the algorithm has also been discussed. When processing image sequences, two consecutive images often exhibit strong similarities. Therefore, the corresponding luminal contours are often close to one another. Taking advantage of the contour location information in an image [i] to segment the luminal border in the image $[\mathrm{i}+1]$ is very suitable. This is performed by using the final contour in the image [i] as the initial contour for the image $[\mathrm{i}+1]$. This eases and accelerates the snake convergence to the right contour.

Owing to the particular objective of this study, only the segmentation of the luminal boundary has been considered. This method can be naturally extended to the detection of the media-adventitia interface, necessary for the assessment of the plaque dimensions and of the degree of vessel stenosis. In practical terms, once having determined the position of the blood-tissue interface, the luminal area will be excluded and the second contour will be searched in the remaining region, as a continuous smooth closed curve that evolves according to the statistics of the image. The fully automatic character of the method should be preserved.

In this paper, the cases of totally occlusive plaques, dissections and side-branches were not considered. Future objectives are directed toward an improvement of the algorithm, such that it can process successfully any of these particular cases.

Acknowledgment

The help of D. Goertz in the manuscript preparation was highly appreciated.

References

[1] *The Vulnerable Atherosclerotic Plaque: Understanding, Identification and Modification*, V. Fuster, Ed., Amer. Heart Assoc., New-York, 1999, p. 429.

[2] D. Y. Lee, N. Eigler, H. luo, T. Nishioka, S. Tabak, J. S. Forrester, and R. J. Siegel, "Effects of intracoronary ultrasound imaging on clinical decision making," *Amer. Heart J.*, vol. 129, no. 6, pp. 1084–93, 1995.

[3] P. R. Liebson and L. W. Klein, "Intravascular ultrasound in coronary atherosclerosis: A new approach to clinical assessment," *Amer. Heart J.*, vol. 123, pp. 1643–1660, 1991.

[4] J. Ophir, I. Céspedes, H. Ponnekanti, Y. Yazdi, and X. Li, "Elastography: A quantitative method for imaging the elasticity of biological tissues," *Ultrason. Imag.*, vol. 13, pp. 111–134, 1991.

[5] M. O'Donnell, A. R. Skovoroda, B. M. Shapo, and S. Y. Emelianov, "Internal displacement and strain imaging using ultrasonic speckle tracking," *IEEE Trans. Ultrason, Ferroelect., Freq. Contr.*, vol. 44, no. 3, pp. 714–721, 1994.

[6] E. Brusseau, J. Fromageau, G. Finet, P. Delachartre, and D. Vray, "Axial strain imaging of intravascular data: Results on polyvinyl alcohol cryogel phantoms and a carotid artery," *Ultrasound Med. Biol.*, vol. 27, no. 12, pp. 1631–1642, 2001.

[7] C. L. de Korte, G. Pasterkamp, A. F. W. van der Steen, H. A. Woutman, and N. Bom, "Characterization of plaque components with intravascular ultrasound elastography in human femoral and coronary arteries in vitro," *Circulation*, vol. 102, no. 6, pp. 617–23, 2000.

[8] P. D. Richardson, M. J. Davies, and G. V. R. Born, "Influence of plaque configuration and stress distribution on fissuring of coronary atherosclerotic plaque," *Lancet*, vol. 2, pp. 941–944, 1989.

[9] R. T. Lee, A. J. Grodzinsky, E. H. Frank, R. D. Kamm, and F. J. Schoen, "Structure-dependent dynamic mechanical behavior of fibrous caps from human atherosclerotic plaques," *Circulation*, vol. 83, pp. 1764–1770, 1991.

[10] C. L. Lendon, M. J. Davies, G. V. Born, and P. D. Richardson, "Atherosclerotic plaque caps are locally weakened when macrophage density is increased," *Atherosclerosis*, vol. 87, pp. 87–90, 1991.

[11] Y. C. Fung, *Biomechanical Properties of Living Tissues*, 2nd ed. New York: Springer-Verlag, 1993, p. 568.

[12] C. L. de Korte, A. F. W. van der Steen, E. I. Cespedes, G. Pasterkamp, S. G. Carlier, F. Mastik, A. H. Schoneveld, P. W. Serruys, and N. Bom, "Characterization of plaque components and vulnerability with intravascular ultrasound elastography," *Phys. Med. Biol.*, vol. 45, no. 6, pp. 1465–75, 2000.

[13] A. K. Jain, *Fundamentals of Digital Image Processing*. Englewood Cliffs, NJ: Prentice-Hall, 1989.

[14] W. Li, A. F. W. van der Steen, C. T. Lancee, J. Honkoop, E. J. Gussenhover, and N. Bom, "Temporal correlation of blood scattering signals in vivo from radiofrequency intravascular ultrasound," *Ultrasound Med. Biol.*, vol. 22, no. 5, pp. 583–90, 1996.

[15] D. Adam, O. Hareuveni, and S. Sideman, "Semiautomatic border tracking of cine echocardiography ventricular images," *IEEE Trans. Med. Imag.*, vol. MI-6, pp. 266–71, June 1987.

[16] D. M. Herrington, T. Johnson, P. Santago, and W. E. Sydner, "Semi-automated boundary detection for intravascular ultrasound," in *Proc. Computers in Cardiology*, vol. 192, 1992, pp. 103–106.

[17] W. Li, C. von Birgelen, C. Di Mario, E. Boersma, E. J. Gussenhoven, N. H. J. J. van der Putten, and N. Bom, "Semi-automatic contour detection for volumetric quantification of intravascular ultrasound," in *Proc. Computers in Cardiology 1994*, 1994/95, pp. 277–280.

[18] W. Li, J. G. Bosch, Y. Zhong, W. J. Gussenhoven, H. Rijsterborgh, J. H. C. Rieber, and N. Bom, "Semiautomatic frame-to-frame tracking of the luminal border from intravascular ultrasound," in *Proc. Computers in Cardiology 1991*, 1991, pp. 353–356.

[19] S. D. Ollabariaga and A. W. M. Smeulders, "Interaction in the segmentation of medical images: A survey," *Med. Image Anal.*, vol. 5, no. 2, pp. 1027–1042, 2001.

[20] I. Wolf, M. Hastenteufel, R. De Simone, M. Vetter, G. Glombitza, S. Mottl-Link, C. F. Vahl, and H.-P. Meinzer, "ROPES: A semi-automated segmentation method for accelerated analysis of three-dimensional echocardiographic data," *IEEE Trans. Med. Imag.*, vol. 21, pp. 1091–1104, Sept. 2002.

[21] J. H. Dwyer, P. Sun, H. Kwong-Fu, K. M. Dwyer, and R. Selzer, "Automated intima-media thickness: The Los Angeles atherosclerosis study," *Ultrasound Med. Biol.*, vol. 24, no. 7, pp. 981–987, 1998.

[22] G. Koning, J. Dijkstra, C. von Birgelen, J. C. Tuinenburg, J. Brunette, J. C. Tardif, P. W. Oemrawsingh, C. Sieling, S. Melsa, and J. H. Reiber, "Advanced contour detection for three-dimensional intracoronary ultrasound: A validation—In vitro and in vivo," *Int. J. Cardiovasc. Imag.*, vol. 18, no. 4, pp. 235–48, 2002.

[23] M. Sonka, X. Zhang, M. Siebes, M. S. Bissing, S. C. DeJong, S. M. Collins, and C. R. McKay, "Segmentation of intravascular ultrasound images: A knowledge-based approach," *IEEE Trans. Med. Imag.*, vol. 14, pp. 719–732, Aug. 1995.

[24] X. Zhang, C. R. McKay, and M. Sonka, "Tissue characterization in intravascular ultrasound images," *IEEE Trans. Med. Imag.*, vol. 17, pp. 889–899, Dec 1998.

[25] A. Wahle, G. P. M. Prause, S. C. DeJong, and M. Sonka, "Geometrically correct 3-D reconstruction of intravascular ultrasound images by fusion with biplane angiography—Methods and validation," *IEEE Trans. Med. Imag.*, vol. 18, pp. 686–699, Aug. 1999.

[26] M. Kass, A. Witkin, and D. Terzopoulos, "Snakes: Active contour models," *Int. J. Comput. Vis.*, vol. 1, no. 4, pp. 321–331, 1988.

[27] T. McInerney and D. Terzopoulos, "Deformable models in medical image analysis: A survey," *Med. Image Anal.*, vol. 1, no. 2, pp. 91–108, 1996.

[28] T. Cootes, A. Hill, C. J. Taylor, and J. Haslam, "Use of active models for locating structure in medical images," *Image Vis. Computing*, vol. 12, pp. 355–365, 1994.

[29] A. Chakraborty, L. H. Staib, and J. S. Duncan, "Deformable boundary finding in medical images by integrating gradient and region information," *IEEE Trans Med Imag.*, vol. 15, pp. 859–870, Dec. 1996.

[30] L. D. Cohen, "On active contour models and balloons," *CVGIP: Image Understanding*, vol. 53, no. 2, pp. 211–218, 1991.

[31] G. Kovalski, R. Beyar, R. Shofti, and H. Azhari, "Three-dimensional automatic quantitative analysis of intravascular ultrasound images," *Ultrasound Med. Biol.*, vol. 26, no. 4, pp. 527–537, 2000.

[32] C. Haas, H. Ermert, S. Holt, P. Grewe, A. Machraoui, and J. Barmeyer, "Segmentation of 3D intravascular ultrasonic images based on a random field model," *Ultrasound Med. Biol.*, vol. 26, no. 2, pp. 297–306, 2000.

[33] F. Guérault, P. Delachartre, G. Finet, and I. E. Magnin, "Modélization et segmentation d'images échographiques endovasculaires," *Traitement du Signal*, vol. 17, no. 5/6, pp. 517–529, 2000.

[34] C. Chesnaud, P. Réfrégier, and V. Boulet, "Statistical region snake-based segmentation adapted to physical noise model," *IEEE Trans. Pattern Anal. Machine Intell.*, vol. 21, pp. 1145–1157, Nov. 1999.

[35] R. F. Wagner, S. W. Smith, J. M. Sandrik, and H. Lopez, "Statistics of speckle in ultrasound B-scans," *IEEE Trans. Sonics Ultrason*, vol. SU-30, pp. 156–163, 1983.

[36] R. Wagner, M. Insana, and D. Brown, "Statistical properties of radio-frequency and envelope detected signals with applications to medical ultrasound," *J. Opt. Soc. Amer.*, vol. 4, pp. 910–922, 1987.

[37] J. M. B. Dias and J. M. N. Leitao, "Wall position and thickness estimation from sequences of echocardiographic images," *IEEE Trans. Med Imag.*, vol. 15, pp. 25–38, Feb. 1996.

[38] S. Menet, P. Saint-Marc, and G. Medioni, "B-snakes: Implementation and application in stereo," in *Proc. 7th Israeli Conf. Artificial Intelligence and Computer Vision*, 1991, pp. 223–236.

[39] C. Chesnaud and P. Réfrégier, "Optimal snake region-based segmentation for different physical noise models and fast algorithm implementation," in *Proc. Physics in Signal and Image Processing (PSIP'99)*, Paris, France, 1999, pp. 3–11.

[40] T. F. Cootes, D. Cooper, C. J. Taylor, and J. Graham, "Active shape models—Their training and application," *Comput. Vis. Image Understanding*, vol. 61, no. 1, pp. 38–59, 1995.

[41] V. Dutt, "Statistical Analysis of Ultrasound Echo Envelope," Ph.D. dissertation, The Mayo Graduate School, 1995.

[42] K. A. Wear, R. F. Wagner, D. G. Brown, and M. F. Insana, "Statistical properties of estimates of signal-to-noise ratio and number of scatterers per resolution cell," *J. Acoust. Soc. Amer.*, vol. 102, no. 1, pp. 635–641, 1997.

[43] J.-F. Chen, J. A. Zagzebski, and E. L. Madsen, "Non-Gaussian versus non-Rayleigh statistical properties of ultrasound echo signals," *IEEE Trans. Ultrason., Ferroelect., Freq. Contr.*, vol. 41, pp. 435–440, July 1994.

[44] D. Kaplan and Q. Ma, "On the statistical characteristics of log-compressed Rayleigh signals: Theoretical formulation and experimental results," *J. Acoust. Soc. Amer.*, vol. 95, no. 3, pp. 1396–1400, 1994.

[45] V. Dutt and J. Greenleaf, "Statistics of the log-compressed echo envelope," *J. Acoust. Soc. Amer.*, vol. 99, no. 6, pp. 3817–3825, 1996.

[46] E. Jakeman and R. J. A. Tough, "Generalized K distribution: A statistical model for weak scattering," *J. Opt. Soc. Amer.*, vol. 4, pp. 1764–1772, Sept. 1987.

[47] R. C. Molthen, V. M. Narayanan, P. M. Shankar, J. M. reid, V. Genis, and L. Vergara-Dominguez, "Ultrasound echo evaluation by K-distribution," in *Proc. IEEE Ultrasonics Symp.*, New-York, 1993, pp. 957–960.

[48] L. Weng, J. M. Reid, P. M. Shankar, and K. Soetanto, "Ultrasound speckle analysis based on the K-distribution," *J. Acoust. Soc. Amer.*, vol. 89, no. 6, pp. 2992–2995, 1991.

[49] F. Ossant, F. Patat, M. Lebertre, M.-L. Teriierooiterai, and L. Pourcelot, "Effective density estimators based on the K distribution: Interest of low and fractional order moments," *Ultrason Imag,*, vol. 20, pp. 243–259, 1998.

[50] P. M. Shankar, J. M. Reid, H. Ortega, C. W. Piccoli, and B. B. Goldberg, "Use of non- Rayleigh statistics for the identification of tumors in ultrasonics B-scans of breast," *IEEE Trans. Med. Imag.*, vol. 12, no. 4, pp. 687–692, 1993.

[51] J. C. Bamber, "Attenuation and absorption," in *Physical Principles of Medical Ultrasonics*, C. R. Hill, Ed. New York: Halsted, 1986, p. 495.

[52] F. Dunn, P. D. Edmonds, and W. J. Fry, "Absorption and dispersion of ultrasound ," in *Biological Media in Biological Engineering*. New York: McGraw-Hill, 1969, pp. 205–332.